

# Thermal Runaway and Microwave Heating in Thin Cylindrical Domains

Michael J. Ward <sup>1</sup>

## Abstract

The behavior of the solution to two nonlinear heating problems in a thin cylinder of revolution of variable cross-sectional area is analyzed using asymptotic and numerical methods. The first problem is to calculate the fold point, corresponding to the onset of thermal runaway, for a steady-state nonlinear elliptic equation that arises in combustion theory. In the limit of thin cylindrical domains, it is shown that the onset of thermal runaway can be delayed when a circular cylindrical domain is perturbed into a dumbbell shape. Numerical values for the fold point for different domain shapes are obtained asymptotically and numerically. The second problem that is analyzed is a nonlinear parabolic equation modeling the microwave heating of a ceramic cylinder by a known electric field. The basic model in a thin circular cylindrical domain was analyzed in Booty and Kriegsmann [Methods Appl. Anal., Vol. 4, No. 1, (1994), p. 403]. Their analysis is extended to treat thin cylindrical domains of variable cross-section. It is shown that the steady-state and dynamic behavior of localized regions of high temperature, called hot-spots, depend on a competition between the maxima of the electric field and the maximum deformation of the circular cylinder. For a dumbbell-shaped region it is shown that two disconnected hot-spot regions can occur. Depending on the parameters in the model, these regions, ultimately, either merge as time increases or else remain as disconnected regions for all time.

## 1 Introduction

The behavior of the solution to two nonlinear heating problems in a thin cylinder of revolution of variable cross-sectional area is analyzed using asymptotic and numerical methods.

The first problem is to determine the conditions for the onset of thermal runaway of an exothermically active material contained in a long cylinder of revolution. The cross-sectional shape of the cylinder is given by  $R = R_0g(Z/L)$ , where  $L$  is the length of the cylinder,  $R_0$  is a typical radius of the cross-section, and  $g(z) > 0$  is a dimensionless function. A typical plot of the cylinder is shown in Fig. 1. The dimensional steady-state temperature  $U(Z, R)$  is taken to satisfy

$$U_{ZZ} + U_{RR} + \frac{1}{R}U_R + F(U) = 0, \quad 0 < R < R_0g(Z/L), \quad 0 < Z < L, \quad (1.1a)$$

$$U(0, R) = U_0 u_a(R/R_0), \quad U(L, R) = U_0 u_b(R/R_0), \quad (1.1b)$$

$$U_n + BU = 0, \quad \text{on } R = R_0g(Z/L). \quad (1.1c)$$

---

<sup>1</sup>Department of Mathematics, University of British Columbia, Vancouver, Canada V6T 1Z2

Here  $B > 0$  is the Biot number,  $U_n$  denotes the outward normal derivative, and  $U_0$  is a typical temperature at the ends of the cylinder. The temperature distribution at the ends of the cylinder, given in (1.1b), is allowed to be nonuniform. These boundary conditions at the ends of the cylinder are chosen only for convenience. As remarked following equation (2.12) below, we could also allow boundary conditions that model partial insulation. The reaction is modeled by an Arrhenius-type heat generation term  $F(U)$ . The precise dimensionless form for  $F(U)$  is given in (2.1) below.

For a certain range of parameters, there can be multiple solutions to (1.1) and the corresponding response diagram can be S-shaped. The lower fold point on the response diagram corresponds to the onset of thermal runaway. Our goal is to determine how this point depends on the shape of the cross-section of a cylindrical domain when the domain is thin and the Biot number  $B$  is small. In §2 we introduce an appropriate nondimensionalization of (1.1). In the asymptotic limit of a thin domain and small Biot number, similar to the asymptotic limit considered in [4], we derive an asymptotic nonlinear differential equation for the nondimensional temperature  $u$ . This differential equation has variable coefficients that depend on the cross-sectional radius  $g(z)$ . In §2.1 we outline some previous results of [2], [8], [10], and [15] for the bifurcation diagram associated with this differential equation in a straight circular cylinder where  $g(z) \equiv 1$ . In §2.2 we use asymptotic and numerical methods to compute the lower fold point for different cross-sectional shapes of the cylinder. Typically one might expect that the onset of thermal runaway is hastened when the cross-sectional area is increased since more heat can be generated internally. However, we show that the onset of thermal runaway can in fact be delayed when a circular cylindrical domain is deformed into a dumbbell shape, even though the cross-sectional area is increased at each point along the axis of the cylinder.

The second problem that we analyze is a time-dependent nonlinear diffusive problem that arises when modeling the microwave heating of ceramic fibers in a cylindrical domain of variable cross-sectional area. The basic model in a cylinder of constant cross-section was first introduced in [4]. Following [4], the dimensional model problem for the temperature  $T = T(R, Z, t)$  in the ceramic cylinder of revolution  $0 < Z < L$ ,  $0 < R < R_0g(Z/L)$  is

$$\frac{\partial}{\partial t} (\rho C_\rho T) = \nabla \cdot [K \nabla T] + \frac{\sigma(T)}{2} E_0^2 \sin^2(\pi Z/L). \quad (1.2)$$

One of the key assumptions of the model of [4] is that the electric field  $E(Z) \equiv E_0 \sin(\pi Z/L)$  is known independent of the temperature. The boundary conditions and the initial condition for (1.2) are

$$K \frac{\partial T}{\partial n} + h(T - T_a) + s e(T^4 - T_a^4) = 0, \quad \text{on } R = R_0g(Z/L), \quad (1.3a)$$

$$T(R, 0, t) = T_a, \quad T(R, L, t) = T_a, \quad T(R, Z, 0) = T_a. \quad (1.3b)$$

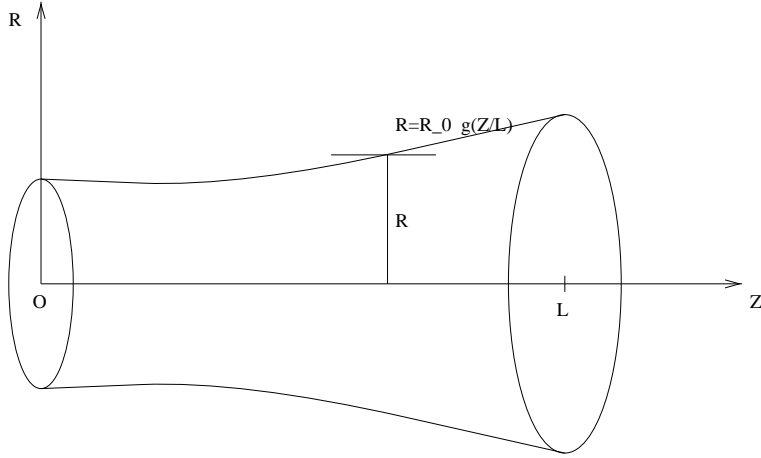


Figure 1: Plot of a typical cylinder of revolution.

In (1.2) and (1.3),  $C_\rho$  is the specific heat,  $\rho$  is the density,  $K$  is the thermal conductivity,  $\sigma$  is the effective electrical conductivity,  $h$  is the surface heat transfer coefficient,  $e$  is the emissivity of the surface,  $s$  is a radiative heat loss parameter,  $T_a$  is the ambient temperature,  $E_0$  is the intensity of the electric field, and  $R_0$  is a typical cross-sectional radius. The functions  $\rho$ ,  $C_\rho$ ,  $K$ , and  $\sigma$  are assumed to depend on the temperature  $T$ , with  $\sigma$  having an Arrhenius-type dependence on  $T$ .

The model (1.2) and (1.3) of [4] is the simplest model of microwave heating. However, it has two main physical limitations that are associated with very high temperature phenomena. Firstly, it assumes that the electric field is given, thereby neglecting the influence of the temperature field on the electric field. This reverse coupling effect, which arises through the temperature dependent coefficients in Maxwell's equations, should be important for very high temperatures (cf. [11], [14]). For a semi-infinite waveguide this aspect has been studied in [14] in the asymptotic WKB limit where the electrical conductivity is small compared to the microwave frequency. The other limitation of this model is that an Arrhenius-type dependence of the conductivity on the temperature is appropriate only when the temperature is not too large. Thus, the saturation of the Arrhenius nonlinearity should not be the mechanism by which the hot-spot is stabilized. Typically, the Arrhenius form for the conductivity should be replaced by a simple exponential function of the temperature (cf. [11]). With this modified form for the conductivity, and at very large temperatures, it was shown in [11] that it is a cavity detuning effect that stabilizes a hot-spot solution. This detuning effect leads to a nonlocal reaction-diffusion equation for the temperature. Some theoretical aspects of this nonlocal reaction-diffusion equation is studied in [5].

In the limit of a thin domain and a small Biot number, a solution to (1.2) and (1.3) was

constructed asymptotically in [4] that had a slowly propagating region (i. e. a hot-spot) where the temperature was very high. Our goal is to extend their analysis to a cylindrical domain of variable cross-section and to determine the effect of the variable cross-sectional area on the evolution of such a hot-spot. In §3 we nondimensionalize (1.2) and (1.3). In the limit of a thin domain and small Biot number, we derive a nonlinear heat equation for the nondimensional temperature  $u$  of the form

$$[(u + 1)\Gamma]_t = \frac{\varepsilon^2}{g^2} [\kappa g^2 v_z]_z + h(z, u), \quad 0 < z < 1; \quad u(0, t) = u(1, t) = u(z, 0) = 0. \quad (1.4)$$

Here  $\Gamma$  and  $\kappa$  are positive functions of  $u$ , and  $h(z, u)$  is a certain function that depends on the electric field, on  $g(z)$ , and on  $u$ . Since the hot-spot region is not adjacent to either of the two ends of the cylinder, the precise boundary condition that we choose at the ends of the cylinder is not critical to the analysis. In particular, the insulating boundary conditions on  $z = 0$  and  $z = 1$  taken in [4] leads to the same results for the hot-spot evolution.

In §3.1 and §3.2 we show that the steady-state and dynamic behavior of hot-spots for (1.4) depend on a competition between the maximum of the electric field and the maximum deformation of the circular cylinder. The tendency of the electric field is to try to generate a hot-spot region near its maximum value, which occurs at the midpoint  $z = 1/2$ . However, if the electric field was spatially constant, a hot-spot would develop in a region where the cylinder was thick enough. Thus, an interesting competition can arise when a circular cylinder is perturbed into a dumbbell-shape. For such a domain, it is shown in §3.2 that two disconnected hot-spot regions can occur. Thin diffusive interfaces, which propagate slowly in time, provide the transitions between the low and high temperature regions. By determining how these interfaces propagate, we show that these hot-spot regions, ultimately, either merge as time increases or else remain as disconnected regions for all time. Specific conditions that determine which of these two distinct behaviors will occur are derived. This behavior is qualitatively similar to the well-known phenomena of diffusive wave-blocking that has been studied in [3], [7], [13] (see also the references therein) for certain other spatially variable coefficient nonlinear problems of the form (1.4).

## 2 Thermal Runaway in a Long Cylinder of Revolution

We begin by introducing appropriate dimensionless variables for (1.1) under the assumption that the cylinder is long (i. e.  $R_0/L \ll 1$ ) and that the cross-section of the cylinder is nearly insulating (i. e.  $BR_0 \ll 1$ ). A similar asymptotic limit for the microwave heating problem was considered in

[4]. We first introduce a dimensionless heat generation term  $f(u)$  defined by

$$f(u) = F(U_0 u)/F_0 \equiv \exp \left[ \frac{u}{(1 + \beta u)} \right]. \quad (2.1)$$

Here  $\beta > 0$  is the dimensionless activation energy parameter and  $F_0$  is a measure of the heat generation, which depends on the material under consideration. We then introduce dimensionless variables by

$$z = Z/L, \quad r = R/R_0, \quad u = U/U_0, \quad \varepsilon = R_0/L, \quad (2.2)$$

where  $\varepsilon \ll 1$ . In terms of these new variables, (1.1) becomes

$$\varepsilon^2 u_{zz} + u_{rr} + \frac{1}{r} u_r + \frac{F_0 R_0^2}{U_0} f(u) = 0, \quad 0 < r < g(z), \quad 0 < z < 1, \quad (2.3a)$$

$$u(0, r) = u_a(r), \quad u(1, r) = u_b(r), \quad (2.3b)$$

$$u_r - \varepsilon^2 g'(z) u_z + R_0 B \left( 1 + \varepsilon^2 [g'(z)]^2 \right)^{1/2} u = 0, \quad \text{on } r = g(z). \quad (2.3c)$$

In order for there to be a nontrivial solution to (2.3) we require that the generation of heat inside the cylinder is balanced by the diffusion of heat along the length of the cylinder. In addition, we will assume that the boundary of the cylinder is nearly insulating. Hence, we take

$$R_0 B = \varepsilon^2 b, \quad \frac{F_0 R_0^2}{U_0} = \varepsilon^2 \Lambda, \quad (2.3d)$$

for some  $b$  and  $\Lambda$  that are  $O(1)$  as  $\varepsilon \rightarrow 0$ . Thus, (2.3) becomes

$$\varepsilon^2 u_{zz} + u_{rr} + \frac{1}{r} u_r + \varepsilon^2 \Lambda f(u) = 0, \quad 0 < r < g(z), \quad 0 < z < 1, \quad (2.4a)$$

$$u(0, r) = u_a(r), \quad u(1, r) = u_b(r), \quad (2.4b)$$

$$u_r - \varepsilon^2 g'(z) u_z + \varepsilon^2 b \left( 1 + \varepsilon^2 [g'(z)]^2 \right)^{1/2} u = 0, \quad \text{on } r = g(z). \quad (2.4c)$$

Finally, a convenient measure of the norm of the solution is given by

$$\alpha = \int_0^1 \int_0^{g(z)} u^2 r \, dr \, dz. \quad (2.5)$$

The type of domains that we will consider are those for which  $g(0) = g(1) = 1$ ,  $g(z) > 0$  for  $0 < z < 1$ , and  $g(z)$  is an even function about the midpoint value  $z = 1/2$ .

We now calculate the solution branch  $u = u(z, r; \alpha, \varepsilon)$ ,  $\Lambda = \Lambda(\alpha; \varepsilon)$  in the limit  $\varepsilon \rightarrow 0$ . For strictly one-dimensional problems where  $g(z) \equiv 1$  and  $b = 0$  it is well-known that the graph of  $\alpha$  versus  $\Lambda$  can be S-shaped having two simple fold points (cf. [2]). The lower fold point represents the ignition point for the onset of thermal runaway. Our main goal is to calculate the ignition point for (2.4) in the limit  $\varepsilon \rightarrow 0$ .

The problem (2.4) is a singular perturbation problem with an outer region defined away from the ends of the cylinder and with inner regions defined near the ends of the cylinder. To analyze this boundary layer structure for (2.4), we use a singular perturbation method of a type similar to that used in section 3.3 of [9] to study the asymptotic behavior of a linear heat equation in a thin cylindrical domain.

For a fixed value of  $\alpha$ , the solution to (2.4) in the outer region is expanded as

$$u = v(z, r) + \varepsilon^2 u_1(z, r) + \cdots, \quad \Lambda = \lambda + \varepsilon^2 \lambda_1 + \cdots. \quad (2.6)$$

Substituting (2.6) into (2.4a) and (2.4c), we obtain the  $O(1)$  problem

$$Lv \equiv v_{rr} + \frac{1}{r} v_r = 0, \quad 0 < r < g(z); \quad v_r = 0, \quad \text{on } r = g(z). \quad (2.7)$$

From (2.7), we conclude that  $v = v(z)$ . The  $O(\varepsilon^2)$  problem is

$$Lu_1 = -v'' - \lambda f(v), \quad 0 < r < g(z), \quad (2.8a)$$

$$u_{1r} = g'(z)v' - bv, \quad \text{on } r = g(z). \quad (2.8b)$$

Since  $L1 = 0$ , (2.8) must satisfy a solvability condition. This condition yields a differential equation for  $v(z)$ . To derive this equation, we integrate (2.8a) and use the boundary condition (2.8b). Then, we substitute  $u \sim v$  into (2.5) to calculate  $\alpha$ . In this way, we obtain the following problem for  $v(z; \alpha)$ :

$$\left( [g(z)]^2 v' \right)' + [g(z)]^2 \lambda f(v) = 2g(z)bv, \quad (2.9a)$$

$$\alpha = \frac{1}{2} \int_0^1 v^2 [g(z)]^2 dz. \quad (2.9b)$$

To obtain effective boundary conditions for  $v$ , we need to insert boundary layers near the ends of the cylinder. Near  $z = 0$ , we introduce the new variables  $y = \varepsilon^{-1}z$ ,  $\tilde{u}(y, r) = u(\varepsilon y, r)$ , and we expand  $\tilde{u} = \tilde{u}_0 + O(\varepsilon^2)$ . From (2.3), we find that  $\tilde{u}_0(y, r)$  satisfies

$$\tilde{u}_{0yy} + L\tilde{u}_0 = 0, \quad 0 < r < g_0, \quad 0 < y < \infty; \quad \tilde{u}_0(0, r) = u_a(r); \quad \tilde{u}_{0r}(g_0, y) = 0, \quad (2.10)$$

where  $g_0 \equiv g(0)$ . By separating variables, we calculate the solution to (2.10) as

$$\tilde{u}_0(y, r) = A_0 + \sum_{n=0}^{\infty} A_n J_0(\kappa_n r/g_0) e^{-\kappa_n^2 y/g_0^2}, \quad (2.11a)$$

where  $J_0(z)$  is the usual Bessel function of order zero. Here  $\kappa_n$ , for  $n \geq 1$ , are the roots of  $J_0'(z) = 0$ . The constants  $A_0$  and  $A_n$  for  $n \geq 1$  are given by

$$A_0 = \frac{2}{g_0^2} \int_0^{g_0} r u_a(r) dr, \quad A_n = \int_0^{g_0} r u_a(r) J_0(\kappa_n r/g_0) dr \left( \int_0^{g_0} r [J_0(\kappa_n r/g_0)]^2 dr \right)^{-1}. \quad (2.11b)$$

The matching condition is that  $\tilde{u}_0(y, r)$  must agree as  $y \rightarrow \infty$  with  $v(z)$  as  $z \rightarrow 0$ . Thus,  $A_0 = v(0)$ . A similar analysis can be done near the endpoint at  $z = 1$ . The inner solution is now given by (2.11) with  $y = \varepsilon^{-1}(1 - z)$  and with  $u_a$  and  $g_0$  replaced by  $u_b$  and  $g_1 \equiv g(1)$ , respectively. A similar matching condition determines  $v(1)$ . In this way, we get the effective boundary conditions for (2.9)

$$v(0) = \frac{2}{g_0^2} \int_0^{g_0} r u_a(r) dr, \quad v(1) = \frac{2}{g_1^2} \int_0^{g_1} r u_b(r) dr. \quad (2.12)$$

Thus,  $v(0)$  and  $v(1)$  are the average of the temperature distributions at the ends of the cylinder.

The boundary layer analysis has provided effective end conditions for the temperature profile in the middle region of the cylinder. Other types of boundary conditions at the ends of the cylinder could also have been considered. In particular, by allowing for a partially insulating boundary condition at the left end of the cylinder of the form  $u_n + h(u - u_a) = 0$ , only the details of the boundary layer solution near  $y = 0$  would change. The result (2.12) for  $v(0)$  from the matching condition would be the same.

In §2.2 we study the problem for  $v$  given by (2.9) subject to the boundary conditions (2.12). However, before doing so, in §2.1 we review some of the qualitative properties of the solution to (2.9) when  $g(z) \equiv 1$ .

## 2.1 A Circular Cylinder of Constant Radius

In this subsection we assume that we have a circular cylinder of constant radius with  $g(z) \equiv 1$  in (2.9). We also take  $v(0) = v(1) = 0$  as the boundary conditions for (2.9). We let  $v = w$  and  $\lambda = \lambda_0$  be the solution to (2.9) when  $g(z) \equiv 1$ , so that

$$w'' + \lambda_0 f(w) - 2bw = 0, \quad 0 < z < 1, \quad (2.13a)$$

$$\alpha = \frac{1}{2} \int_0^1 w^2 dz; \quad w(0) = w(1) = 0, \quad (2.13b)$$

where  $f(w) = \exp[w/(1 + \beta w)]$ .

We first consider the case where  $b = 0$ . In this case, it is well-known (cf. [2]) that multiple solutions for (2.13) can occur for some range of  $\lambda$ . More specifically, for  $0 < \beta < \beta_c$ , the graph of  $\alpha$  versus  $\lambda_0$  is S-shaped and has exactly two simple fold points. As  $\beta$  tends to the critical value  $\beta_c$ , the simple fold points coalesce producing a higher order cubic fold point. For the slab geometry, the critical value  $\beta_c \approx 0.2458$  has been computed previously using different numerical methods (see [10], [8], [15]). In the special case when  $\beta = 0$ , so that  $f(w) = e^w$ , there are exactly two solutions to (2.13) on the interval  $0 < \lambda_0 < \lambda_0^*$  and no solutions when  $\lambda_0 > \lambda_0^*$ . When  $\beta = 0$ , we can explicitly calculate a one-parameter family of solutions  $w(z; \gamma)$  to (2.13) as

$$w(z; \gamma) = 2 \log \left( \frac{\cosh \gamma}{\cosh [\gamma(2z - 1)]} \right), \quad \lambda_0(\gamma) = 8\gamma^2 \operatorname{sech}^2 \gamma, \quad (2.14a)$$

$$\alpha = \alpha(\gamma) = \frac{1}{2} \int_0^1 [w(z; \gamma)]^2 dz. \quad (2.14b)$$

The unique fold point is located where  $\lambda_{0\gamma}(\gamma^*) = 0$ . This condition yields the following transcendental equation for the critical value  $\gamma^*$ :

$$1 = \gamma^* \tanh \gamma^*. \quad (2.14c)$$

The solution is  $\gamma^* = 1.1997$  and  $\lambda_0(\gamma^*) \equiv \lambda_0^* = 3.5138$ . A numerical computation gives  $\alpha^* \equiv \frac{1}{2} \int_0^1 [w(z; \gamma^*)]^2 \approx 0.35578$ .

For  $\beta > 0$ , or  $b > 0$ , we must compute the solution to (2.13) numerically to determine the ignition point for thermal runaway. To do so, we form an extended system by solving (2.13) together with the following boundary value problem obtained by differentiating (2.13) with respect to  $\alpha$ :

$$w_\alpha'' + \lambda_0 f'(w) w_\alpha - 2b w_\alpha = -\lambda_{0\alpha} f(w), \quad 0 < z < 1, \quad (2.15a)$$

$$1 = \int_0^1 w w_\alpha dz; \quad w_\alpha(0) = w_\alpha(1) = 0. \quad (2.15b)$$

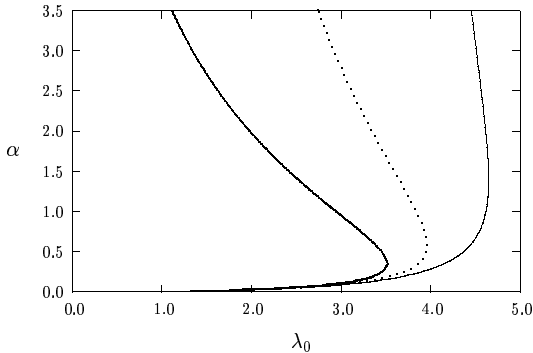
For specific  $b$  and  $\beta$ , (2.13) and (2.15) are solved simultaneously as a function of  $\alpha$  by using the boundary value solver COLSYS [1]. Newton's method is then used to calculate the value  $\alpha = \alpha^*$  at which  $\lambda_{0\alpha}(\alpha^*) = 0$  with  $\lambda_{0\alpha\alpha}(\alpha^*) < 0$ . This determines the ignition point as  $\lambda_0^* \equiv \lambda_0(\alpha^*)$ . We then track this fold point as a function of either  $b$  or  $\beta$  by appending the conditions  $\lambda_{0\alpha}(\alpha^*) = 0$  and  $\lambda_{0\alpha\alpha}(\alpha^*) < 0$  as side constraints in the numerical solution of (2.13) and (2.15). A similar approach was used in [15] to treat a related problem. The limiting result (2.14) for  $\beta = b = 0$  is used to partially check our numerical results. For future reference, as needed below in §2.2, we define  $w^*$

and  $w_\alpha^*$  by

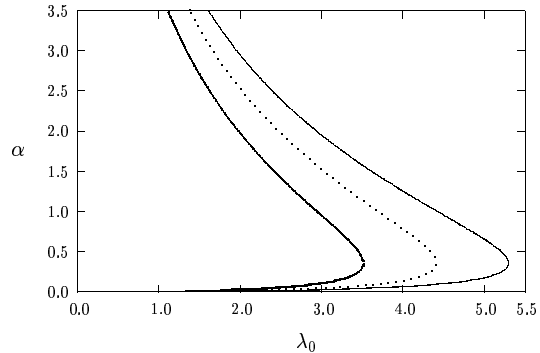
$$w^*(z) \equiv w(z; \alpha^*), \quad w_\alpha^*(z) \equiv \frac{\partial w}{\partial \alpha}(z; \alpha^*). \quad (2.16)$$

In Fig. 2(a) we plot  $\alpha$  versus  $\lambda_0$  near the lower fold point for three values of  $\beta$  when  $b = 0$ . Similar plots are shown in Fig. 2(b) for three values of  $b$  when  $\beta = 0$ . In Fig. 3(a) we plot the lower fold point  $\lambda_0^*$  as a function of  $b$  for three values of  $\beta$ . In Fig. 3(b) we plot the lower fold point on the interval  $\beta \in [0, 0.2]$  for three values of  $b$ . Notice that the fold point value  $\lambda_0^*$  is an increasing function of both  $b$  and  $\beta$ . Thus, as either  $b$  or  $\beta$  is increased, the onset of thermal runaway is delayed. Some particular critical values for  $\lambda_0^*$ , corresponding to the  $y$ -intercepts in Fig. 3(a) and Fig. 3(b), are

$$\begin{aligned} \beta = 0, \quad b = 0, \quad &\rightarrow \quad \lambda_0^* = 3.514; & \beta = 0.1, \quad b = 0, \quad &\rightarrow \quad \lambda_0^* = 3.953; \\ \beta = 0.2, \quad b = 0, \quad &\rightarrow \quad \lambda_0^* = 4.648; & \beta = 0, \quad b = 1.25, \quad &\rightarrow \quad \lambda_0^* = 4.405; \\ & & \beta = 0, \quad b = 2.5, \quad &\rightarrow \quad \lambda_0^* = 5.297. \end{aligned} \quad (2.17)$$



(a)  $b = 0$ ; Three values of  $\beta$ .

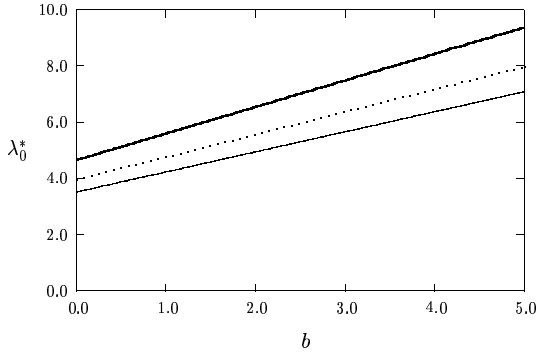


(b)  $\beta = 0$ ; Three values of  $b$ .

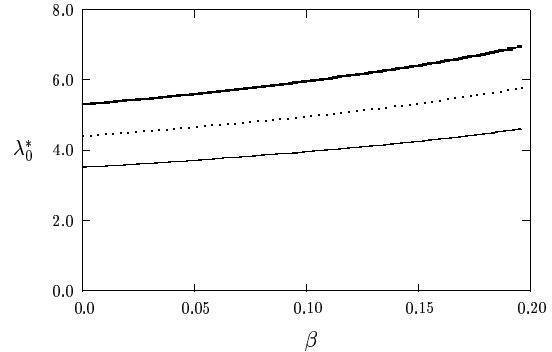
Figure 2: Plots of  $\alpha$  versus  $\lambda_0$  for a circular cylinder of constant cross-section. In Fig. 2a,  $\beta = 0$  is the heavy solid curve,  $\beta = 0.1$  is the dotted curve, and  $\beta = 0.2$  is the solid curve. In Fig. 2b,  $b = 0$  is the heavy solid curve,  $b = 1.25$  is the dotted curve, and  $b = 2.5$  is the solid curve.

## 2.2 Quasi One-Dimensional Nonlinear Heat Conduction

In this subsection we assume that  $g(z) \neq 1$  and that  $v(0) = v(1) = 0$  are the boundary conditions for (2.9). To determine the lower fold point for (2.9) we solve (2.9) numerically together with the



(a) Three values of  $\beta$ .



(b) Three values of  $b$ .

Figure 3: In Fig. 3a we plot  $\lambda_0^*$  versus  $b$  for  $\beta = 0$  (solid curve),  $\beta = 0.1$  (dotted curve), and  $\beta = 0.2$  (heavy solid curve). In Fig. 3b we plot  $\lambda_0^*$  versus  $\beta$  for  $b = 0$  (solid curve),  $b = 1.25$  (dotted curve), and  $b = 2.5$  (heavy solid curve). Each of these plots are for a circular cylinder of constant cross-section.

following boundary value problem obtained by differentiating (2.9) with respect to  $\alpha$ :

$$v_\alpha'' + \lambda f'(v)v_\alpha - \frac{2b}{g}v_\alpha = -\frac{2g'}{g}v_\alpha' - \lambda_\alpha f(v), \quad 0 < z < 1, \quad (2.18a)$$

$$1 = \int_0^1 [g(z)]^2 v v_\alpha dz; \quad v_\alpha(0) = v_\alpha(1) = 0. \quad (2.18b)$$

The numerical computations are done using COLSYS [1]. To determine the lower fold point  $\alpha = \alpha^*$  and  $\lambda^* \equiv \lambda(\alpha^*)$ , we append the side constraints  $\lambda_\alpha(\alpha^*) = 0$  and  $\lambda_{\alpha\alpha}(\alpha^*) < 0$  to this extended system and use Newton's method.

Numerical results for  $\lambda^* \equiv \lambda(\alpha^*)$  are given below for a  $g(z)$  of the form

$$g(z) = 1 + \delta h(z), \quad h(z) \equiv cz(1-z) [\exp(-z_-^2/2\sigma^2) + \exp(-z_+^2/2\sigma^2)], \quad (2.19a)$$

where  $0 \leq \delta \leq 1$ . In (2.19a) we have specified

$$z_\pm \equiv z - \frac{1}{2} \pm a; \quad \int_0^1 [h(z)]^2 dz = 1. \quad (2.19b)$$

The normalization condition in (2.19b) determines  $c = c(a, \sigma)$ . When  $a \approx 0$  the cylinder has a bell-shaped profile centered at  $z = 1/2$ . However, as  $a \rightarrow 1/2$ ,  $g(z)$  has a dumbbell shape where it

is thicker near the ends of the cylinder than in the middle. As we show below, this difference in the shape of the boundary profile has an interesting qualitative effect on the behavior of the fold point. Plots of  $h(z)$  and  $g(z)$  when  $\delta = 0.15$  and  $\sigma = 0.1$  are shown in Fig. 4(a) and Fig. 4(b) for three values of  $a$ .

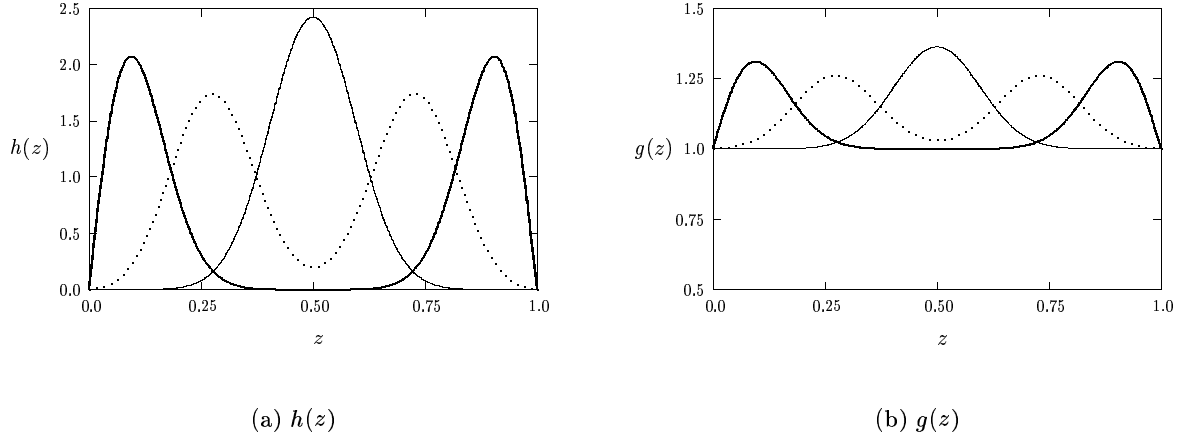


Figure 4: Plots of the functions  $h(z)$  and  $g(z)$  for three values of  $a$  when  $\sigma = 0.1$  and  $\delta = 0.15$ . The heavy solid curve is  $a = 0.5$ , the dotted curve is  $a = 0.25$ , and the solid curve is  $a = 0$ .

To get some analytical insight into the effect of the profile  $g(z)$  on  $\lambda^*$ , we calculate  $\lambda^*$  asymptotically when  $\delta \ll 1$ . For a fixed  $\alpha$ , we expand the solution to (2.9) when  $\delta \ll 1$  as

$$v = w + \delta v_1 + \dots, \quad \lambda = \lambda_0 + \delta \lambda_1 + \dots. \quad (2.20)$$

Substituting (2.20) and  $g(z) = 1 + \delta h(z)$  into (2.9), we obtain that  $w$  and  $\lambda_0$  satisfy (2.13), and that  $v_1$  satisfies

$$L v_1 \equiv v_1'' + \lambda_0 f'(w) v_1 - 2b v_1 = -\lambda_1 f(w) - 2h' w' - 2h b w, \quad (2.21a)$$

$$\int_0^1 w v_1 dz = - \int_0^1 h w^2 dz; \quad v_1(0) = v_1(1) = 0. \quad (2.21b)$$

Let  $\lambda^*$  and  $\lambda_0^* \equiv \lambda_0(\alpha^*)$  denote the fold point locations for the perturbed and the unperturbed ( $\delta = 0$ ) problems, respectively. Then, when  $\delta \ll 1$ , it is easy to see that

$$\lambda^* \sim \lambda_0^* + \delta \lambda_1(\alpha^*) + \dots. \quad (2.22)$$

When  $\alpha = \alpha^*$ , the function  $w_\alpha^*$ , defined in (2.16), is a nontrivial solution to  $Lv_1 = 0$ , where  $L$  is given in (2.21a). Thus, when  $\alpha = \alpha^*$ , the right-hand side of (2.21a) must satisfy the solvability condition that it be orthogonal to  $w_\alpha^*$  with respect to the  $L_2$  inner product. This condition determines  $\lambda_1(\alpha^*)$  as

$$\lambda_1(\alpha^*) \int_0^1 f(w^*) w_\alpha^* dz = -2b \int_0^1 h(z) w^* w_\alpha^* dz - 2 \int_0^1 h' w^{*'} w_\alpha^* dz. \quad (2.23)$$

The second term on the right-hand side of (2.23) is integrated by parts and we use (2.15a) to calculate  $w^{*''}$ . In this way, we obtain

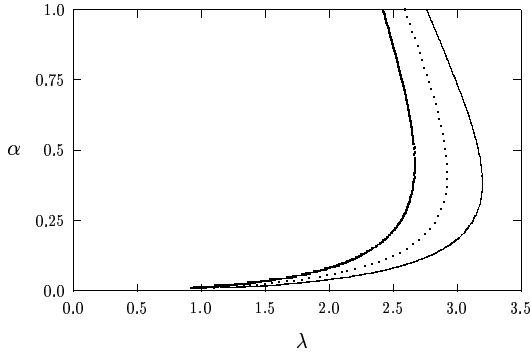
$$\lambda_1(\alpha^*) = \frac{2}{\zeta} \int_0^1 h \left( b w^* w_\alpha^* + w^{*'} w_\alpha^{*'} - \lambda_0^* f(w^*) w_\alpha^* \right) dz, \quad \zeta \equiv \int_0^1 f(w^*) w_\alpha^* dz. \quad (2.24)$$

Substituting (2.24) into (2.22), we obtain the expansion of the fold point when  $\delta \ll 1$  in terms of  $h(z)$  and of the solution to the circular cylinder problem at the unperturbed fold point location. When  $\beta = b = 0$  we can use (2.14) to calculate  $\lambda_1$  explicitly. A simple calculation in this case shows that

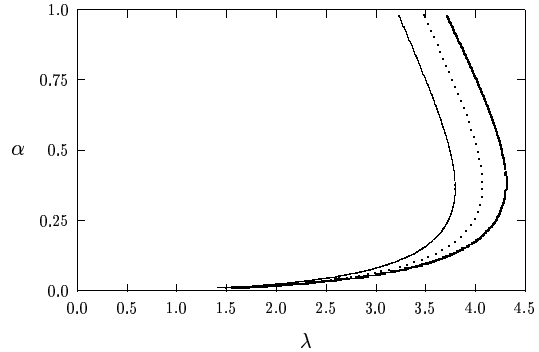
$$\lambda_1(\alpha^*) = \frac{16}{\gamma^*} (\gamma^{*2} - 1) \int_{-\gamma^*}^{\gamma^*} (\tanh^2 \mu - \operatorname{sech}^2 \mu + 2\mu \tanh \mu \operatorname{sech}^2 \mu) h \left[ \frac{1}{2} \left( 1 + \frac{\mu}{\gamma^*} \right) \right] d\mu. \quad (2.25)$$

We now use (2.24) to qualitatively discuss the effect of the boundary perturbation  $h(z)$ , with  $h(z) > 0$ , on the fold point. If  $\lambda_1(\alpha^*) > 0$  ( $\lambda_1(\alpha^*) < 0$ ), then  $h(z)$  has the effect of delaying (advancing) the onset of thermal runaway. There are three integrals that determine the sign of  $\lambda_1(\alpha^*)$  in (2.24). Since  $w_\alpha^* > 0$  and  $w^* > 0$ , the first integral on the right-hand side of (2.24), which is proportional to  $b$ , is positive. This term represents the stabilizing effect of the Robin-type condition on the cylinder boundary. The second integral in (2.24), whose integrand is proportional to  $h w^{*'} w_\alpha^{*'}$  is also positive. This term is a measure of the diffusion of heat along the length of the cylinder and its effect is stabilizing. In contrast, the third integral in (2.24), which is proportional to  $\lambda_0^*$ , is negative. This term represents the production of heat inside the cylinder, and its effect is to destabilize the cylinder. The sign of  $\lambda_1(\alpha^*)$  is determined by a competition between these three terms.

Physically, when  $b = 0$ , an increase in the cross-sectional area of the cylinder allows for an increased heat production generated by the Arrhenius-type heating term. However, the increase in cross-sectional area also allows more of the heat generated internally to diffuse along the length of the cylinder and out from the two ends at  $z = 0$  and  $z = 1$ . This type of competition determines whether the onset of thermal runaway will be advanced or delayed. In particular, suppose that  $a = 0$  in (2.19) so that  $h(z)$  has a single maximum at  $z = 1/2$ . In this case, we would expect



(a)  $a = 0$ ; Three values of  $\delta$ .



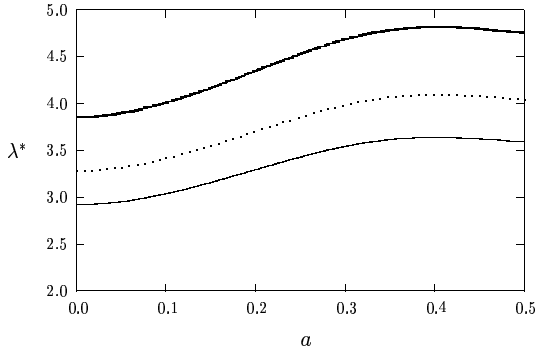
(b)  $a = 0.5$ ; Three values of  $\delta$ .

Figure 5: Plots of  $\alpha$  versus  $\lambda$  for a cylinder of variable cross-section with  $\beta = b = 0$  and  $\sigma = 0.1$ . In each figure, the solid curve corresponds to  $\delta = 0.05$ , the dotted curve corresponds to  $\delta = 0.1$ , and the heavy solid curve corresponds to  $\delta = 0.15$ .

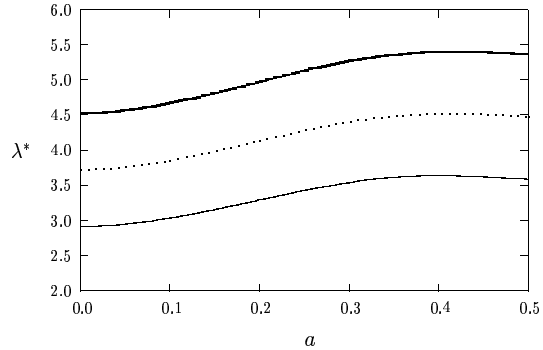
that the increased heat production would dominate the small increase in the ability to diffuse heat towards the ends. However, if  $a \approx 0.5$ , so that  $h(z)$  has a dumbbell shape, we would expect that the increased heat production would be dominated by the stabilizing effect induced by the increased cross-sectional area near the ends of the cylinder. Thus, when  $b = 0$ , we would expect that the onset of thermal runaway is advanced when  $a \approx 0$  and is delayed when  $a \approx 0.5$ . Mathematically, this prediction is based on the observation that, as a function of  $z$ ,  $f(w^*)$  and  $w_\alpha^*$  have maxima at  $z = 1/2$ , whereas  $w^{*'}$  and  $w_\alpha^{*'}$  have maxima at  $z = 0$  and  $z = 1$ . The function  $h(z)$  in (2.24) acts as a weighting function on these quantities.

Our observation that the onset of thermal runaway can be delayed by certain choices of the cross-sectional shape of the cylinder is reminiscent of another paradoxical cooling effect that occurs with a linear steady-state heat equation. For a linear heat equation in a concentric annulus with no sinks or sources present, it is well-known from section 3.3 of [6] that, for an annulus of a sufficiently narrow gap, the effect of adding insulation to the outer boundary of the annulus can increase the heat loss through the boundary and thereby cool the material.

For  $a = 0$  and  $a = 0.5$  we plot in Fig. 5(a) and Fig. 5(b), respectively, the curves  $\alpha$  versus  $\lambda$  for three values of  $\delta$  when  $\beta = b = 0$  and  $\sigma = 0.1$ . The results were obtained from a numerical solution to (2.9) and (2.18) using COLSYS [1]. In Fig. 6(a) we plot the fold point  $\lambda^*$  versus  $a$  for several values of  $\beta$  when  $\delta = \sigma = 0.1$  and  $b = 0$ . A similar plot is shown in Fig. 6(b) for three



(a)  $b = 0$ ; Three values of  $\beta$ .



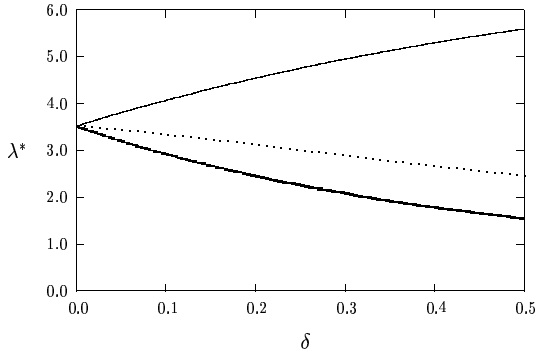
(b)  $\beta = 0$ ; Three values of  $b$ .

Figure 6: Plots of  $\lambda^*$  versus  $a$  for a cylinder of variable cross-section with  $\delta = 0.1$  and  $\sigma = 0.1$ . In Fig. 6a,  $\beta = 0$  is the solid curve,  $\beta = 0.1$  is the dotted curve, and  $\beta = 0.2$  is the heavy solid curve. In Fig. 6b,  $b = 0$  is the solid curve,  $b = 1.25$  is the dotted curve, and  $b = 2.5$  is the heavy solid curve.

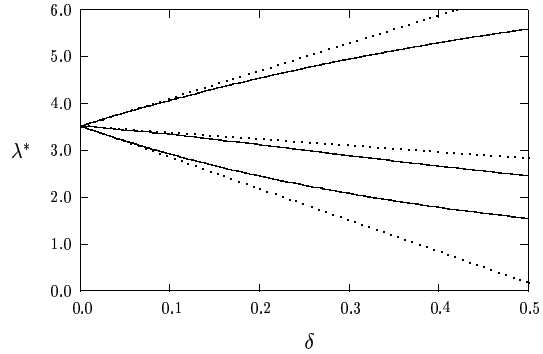
values of  $b$  when  $\beta = 0$ . For each of the plots in Fig. 6(a) and Fig. 6(b), the numerical results for the maximum value of  $\lambda^*$  as a function of  $a$ , denoted by  $\lambda_m^*$ , are

$$\begin{aligned}
 \beta = 0, \quad b = 0; & \quad \lambda_m^* = 3.636 & \text{when } a = 0.39, \\
 \beta = 0.1, \quad b = 0; & \quad \lambda_m^* = 4.091 & \text{when } a = 0.40, \\
 \beta = 0.2, \quad b = 0; & \quad \lambda_m^* = 4.813 & \text{when } a = 0.40, \\
 \beta = 0, \quad b = 1.25; & \quad \lambda_m^* = 4.516 & \text{when } a = 0.41, \\
 \beta = 0, \quad b = 2.5; & \quad \lambda_m^* = 5.398 & \text{when } a = 0.42.
 \end{aligned} \tag{2.26}$$

By comparing (2.17) with (2.26) and Fig. 6(a), 6(b) with the results shown in Fig. 3(a), 3(b), we conclude that the onset of thermal runaway can be delayed for a dumbbell-shaped region. This was anticipated on physical grounds above. In Fig. 7(a) we plot  $\lambda^*$  versus  $\delta$  for three values of  $a$  when  $\sigma = 0.1$  and  $\beta = b = 0$ . The onset of thermal runaway is delayed for the curve in this plot that has a positive slope. Finally, in Fig. 7(b), where  $\sigma = 0.1$  and  $\beta = b = 0$ , we compare the numerical result for the fold point  $\lambda^*$  as a function of  $\delta$  with the corresponding asymptotic result (2.25). The comparisons are made for the values of  $a$  given in Fig. 7(a). The agreement between the full numerical result and the asymptotic formula (2.25) is found to be close when  $\delta \leq 0.2$ .



(a) Three values of  $a$ .



(b)  $\beta = 0$ ; Three values of  $b$ .

Figure 7: In Fig. 7a we plot  $\lambda^*$  versus  $\delta$  for three values of  $a$  when  $\sigma = 0.1$  and  $\beta = b = 0$ . The heavy solid curve is  $a = 0$ , the dotted curve is  $a = 0.25$ , and the solid curve is  $a = 0.5$ . For each of these values of  $a$ , in Fig. 7b we compare the numerical results (solid curves) for  $\lambda^*$  as a function of  $\delta$  with the asymptotic result (2.25) (dotted curves) that is valid for  $\delta \ll 1$ .

### 3 Microwave Heating in a Cylinder of Variable Thickness

Following [4], we now introduce appropriate dimensionless variables for (1.2) and (1.3) under the assumption that the cylinder is long, and that there is little heat escape along the length of the cylinder. In the notation below, we let  $H_a$  denote the quantity  $H$  evaluated at  $T = T_a$ . The dimensionless variables are introduced as follows:

$$z = Z/L, \quad r = R/R_0, \quad u = T/T_a - 1, \quad \eta = h [R_0(\rho C_\rho)_a]^{-1} t, \quad (3.1a)$$

$$\rho C_\rho = (\rho C_\rho)_a \Gamma(u), \quad K = K_a \kappa(u), \quad \sigma = \sigma_a f(u). \quad (3.1b)$$

The dimensionless Biot numbers and the power  $p$  are defined by

$$b = hR_0/K_a, \quad b_1 = seR_0T_a^3/K_a, \quad \alpha = b_1/b, \quad p = \sigma_a R_0 E_0^2 / (2hT_a). \quad (3.1c)$$

As in [4], we assume that  $b \rightarrow 0$  with  $\alpha$  fixed, and that the aspect ratio  $R_0/L \ll 1$  satisfies

$$b \ll \frac{R_0}{L} \ll b^{1/2}, \quad \text{as } b \rightarrow 0. \quad (3.2)$$

Following [4], we write  $R_0/L = \varepsilon b^{1/2}$ , where  $b^{1/2} \ll \varepsilon \ll 1$ . In terms of these dimensionless variables, we obtain from (1.2) that

$$b[(u+1)\Gamma]_\eta = \varepsilon^2 b [\kappa u_z]_z + r^{-1} [r\kappa u_r]_r + pbf \sin^2(\pi z), \quad (3.3a)$$

in  $0 < z < 1$ ,  $0 < r < g(z)$ . The boundary and initial conditions in (1.3a) and (1.3b) transform to

$$\kappa \left( u_r - \varepsilon^2 b g'(z) u_z \right) + b \left( 1 + \varepsilon^2 b [g'(z)]^2 \right)^{1/2} (u + \alpha [(u+1)^4 - 1]) = 0, \quad (3.3b)$$

and

$$u(r, 0, \eta) = 0, \quad u(r, 1, \eta) = 0, \quad u(r, z, 0) = 0. \quad (3.3c)$$

In the analysis below we assume that the dimensionless cross-sectional radius satisfies  $g(0) = g(1) = 1$  and  $g(z) > 0$  for  $0 < z < 1$ . In addition,  $g(z)$  is assumed to be a symmetric function about the midpoint value  $z = 1/2$ .

For  $b \rightarrow 0$ , we expand the solution to (3.3) as

$$u = v + bu_1 + \dots. \quad (3.4)$$

Substituting (3.4) into (3.3a) and (3.3b), we obtain to leading order that

$$[r\kappa v_r]_r = 0, \quad \text{in } 0 < r < g(z); \quad \kappa v_r = 0, \quad \text{on } r = g(z). \quad (3.5)$$

From (3.5) it follows that  $v = v(z, \eta)$ . The problem for  $u_1$ , obtained by collecting the  $O(b)$  terms in the expansion, is

$$r^{-1} [r\kappa u_{1r}]_r = N(v) \equiv -\varepsilon^2 [\kappa v_z]_z + [(v+1)\Gamma]_\eta - pbf \sin^2(\pi z), \quad (3.6a)$$

with boundary condition

$$\kappa u_{1r} = \kappa \varepsilon^2 g'(z) v_z - (v + \alpha [(v+1)^4 - 1]), \quad \text{on } r = g(z). \quad (3.6b)$$

By multiplying (3.6a) by  $r$ , and then integrating in  $r$  from 0 to  $g(z)$ , we get

$$g\kappa u_{1r} \Big|_{r=g(z)} = \frac{1}{2} [g(z)]^2 N(v). \quad (3.7)$$

Finally, by substituting (3.6b) into (3.7), we obtain that  $v(z, \eta)$  satisfies

$$[(v+1)\Gamma]_\eta = \varepsilon^2 [\kappa v_z]_z + pbf \sin^2(\pi z) - \frac{2}{g} (v + \alpha [(v+1)^4 - 1]) + \frac{2g'}{g} \kappa \varepsilon^2 v_z, \quad (3.8)$$

in the domain  $0 < z < 1$ ,  $\eta > 0$ , subject to  $v(0, \eta) = v(1, \eta) = v(z, 0) = 0$ . In (3.8),  $\Gamma$ ,  $\kappa$  and  $f$  are given functions of  $v$ .

It is convenient to express (3.8) in the form

$$[(v+1)\Gamma]_\eta = \frac{\varepsilon^2}{g^2} [\kappa g^2 v_z]_z + [P(z) - G(v)] \frac{f(v)}{g(z)}, \quad (3.9a)$$

$$v(z, 0) = 0; \quad v(0, \eta) = v(1, \eta) = 0. \quad (3.9b)$$

Here we have defined  $P(z)$  and  $G(v)$  by

$$P(z) \equiv pg(z) \sin^2(\pi z), \quad G(v) = 2[f(v)]^{-1} (v + \alpha [(v+1)^4 - 1]). \quad (3.9c)$$

We take the same models for  $\kappa$  and  $f$  as in [4]. They are

$$f(v) = 1 + c_1 e^{-c_2/v}; \quad \kappa(v) = 1 + v^2/2 \quad \text{or} \quad \kappa(v) = e^{-v/2}. \quad (3.9d)$$

where  $c_1 > 0$  and  $c_2 > 0$ . In all of the computations below we take the values  $c_1 = 500$ ,  $c_2 = 13.7$ , and  $\alpha = 0.05$ , as used in [4]. In Fig. 8 we plot  $u$  versus  $G(u)$ . This curve is S-shaped with simple fold points at  $(G_l, u_l)$  and  $(G_m, u_m)$ , where  $u_m > u_l$  and  $G_m < G_l$  (see Fig. 8). We remark that the graph  $u$  versus  $G(u)$  has a similar shape for other parameter values.

In the remainder of the analysis below we will take the form (2.19) for  $g(z)$ . The key parameters for  $g(z)$  in (2.19) are  $a$ ,  $\sigma$ , and  $\delta$ . The properties of  $P(z)$ , inherited from  $g(z)$ , are that  $P(z)$  is symmetric about  $z = 1/2$  and that  $P(0) = P(1) = 0$ . In Fig. 9(a) we plot  $P(z)$  versus  $z$  when  $P(z)$  is monotone on  $(0, 1/2)$ . A similar plot, but for other parameter values, is shown in Fig. 9(b) when  $P(z)$  is not monotone. As discussed below, the monotonicity behavior of  $P(z)$  has a significant effect on the qualitative dynamics of a hot-spot solution. There are two cases to consider. The first case is when  $P(z)$  is monotone increasing on  $(0, 1/2)$ . In this case there can only be one hot-spot region. However, when  $P(z)$  has two maxima on  $(0, 1)$ , such as shown in Fig. 9(b), two different hot-spot regions can occur.

The physical explanation for these two different behaviors is that, in forming a hot-spot region, there is a competition between the maximum of the electric field, which occurs at  $z = 1/2$ , and the regions where the cylinder is thickest. For a straight circular cylinder of uniform thickness, a hot-spot can only develop near  $z = 1/2$  where the electric field is most intense. In Case 1, a hot-spot will still occur near  $z = 1/2$  when the deformation of the boundary of the cylinder is concentrated enough near  $z = 1/2$  to ensure that  $P(z)$  is monotone increasing on  $(0, 1/2)$ . In Case 2, the cylinder boundary is strongly deformed into a dumbbell-shape and is thickest far away from the center region near  $z = 1/2$ . This allows  $P(z)$  to possibly be nonmonotone on  $(0, 1/2)$ . In this case, the tendency to form initial hot-spot regions near the lobes of the dumbbell dominates the

tendency to form a hot-spot near  $z = 1/2$  where the electric field is most intense. Thus, in this case, there can be two initial hot-spot regions.

We now describe the initial formation of a hot-spot for (3.9) and we analyze its subsequent evolution for these two different classes of  $P(z)$ .

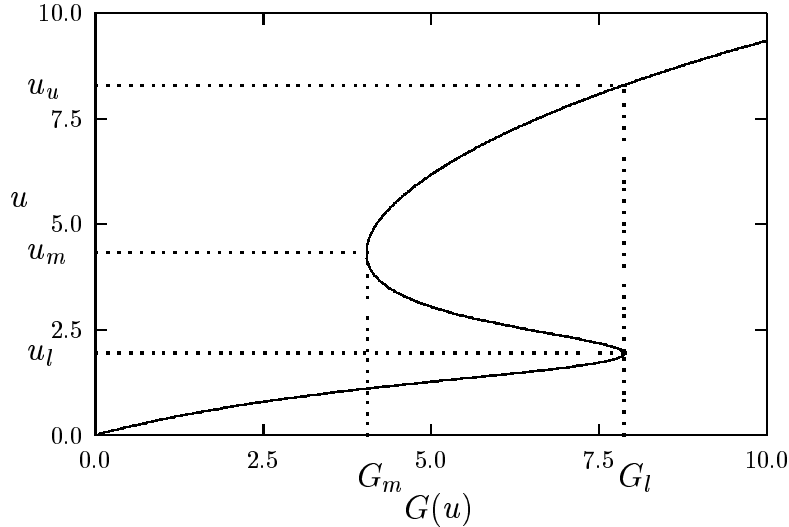


Figure 8: Plot of  $u$  versus  $G(u)$ , defined in (3.9c), where  $f(u) = 1 + 500e^{-13.7/u}$ , and  $\alpha = 0.05$ .

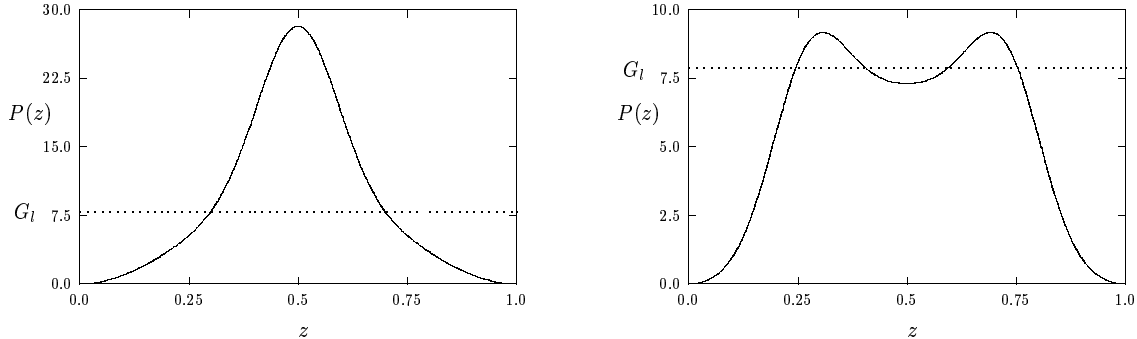
### 3.1 The Hot-Spot Solution: Case 1: $P'(z) > 0$ on $(0, 1/2)$

Assume that  $g(z)$  is such that  $P(z)$  is monotone increasing in  $(0, 1/2)$ , so that  $P(z)$  has its maximum value at  $z = 1/2$ . In particular,  $P(z)$  is monotone increasing on  $(0, 1/2)$  when  $g(z)$  is. However,  $P(z)$  may be also be monotone even when  $g(z)$  is not. A necessary and sufficient condition for  $P(z)$  to be monotone increasing on  $(0, 1/2)$  is that

$$\frac{g'(z)}{g(z)} > -2\pi \cot(\pi z), \quad \text{for } z \in (0, 1/2). \quad (3.10)$$

We first describe the initial formation of the hot-spot. For  $\varepsilon \ll 1$ , and in regions where  $v$  is smooth, we obtain from (3.9a) that

$$[(v+1)\Gamma]_\eta = [P(z) - G(v)] \frac{f(v)}{g(z)}, \quad (3.11)$$



(a) Plot of  $P(z)$  versus  $z$ : Monotone case.

(b) Plot of  $P(z)$  versus  $z$ : NonMonotone case.

Figure 9: In Fig. 9a we plot  $P(z)$ , defined in (3.9c), versus  $z$  when  $p = 10.0$  and when  $g(z)$  has the form given in (2.19) with  $a = 0.0$ ,  $\sigma = 0.1$ , and  $\delta = 0.75$ . In Fig. 9b we plot  $P(z)$  versus  $z$  when  $p = 7.0$ ,  $\sigma = 0.1$ ,  $a = 0.3$ , and  $\delta = 0.75$ . The dotted line in these figures is the value  $G_l$  given in Fig. 8. Initial hot-spot regions correspond to ranges of  $z$  where  $P(z) > G_l$ . These regions, which result from the transient dynamics (3.11), then expand slowly in time on a time-scale  $t = O(\varepsilon^{-1})$ .

with the initial condition  $v = 0$  when  $\eta = 0$ . Assume that  $p$  is such that  $P(1/2) > G_l$  (see Fig. 8). Then, we can define a unique point  $z^* \in (0, 1/2)$  by  $P(z^*) = G_l$  (see Fig. 9(a)). Starting with the initial condition  $v = 0$  at  $\eta = 0$ , we then integrate the initial value problem (3.11) in the time variable  $\eta$ , and let  $\eta \rightarrow \infty$ , to get

$$v(z, \eta) \rightarrow v(z, \infty) \equiv \begin{cases} v_l(z) & 0 < z < z^*, \\ v_u(z) & z^* < z < 1 - z^*, \\ v_l(z) & 1 - z^* < z < 1. \end{cases} \quad (3.12)$$

Here  $v = v_u(z)$  is the upper branch of  $P(z) = G(v)$  for which  $v_u(z) \rightarrow u_u$  as  $z \rightarrow z^*$  (see Fig. 8), and  $v = v_l(z)$  is the lower branch of  $P(z) = G(v)$  with  $v_l(z) \rightarrow u_l$  as  $z \rightarrow z^*$ . The hot-spot initially occupies the region  $z \in (z^*, 1 - z^*)$ , which corresponds to the region in Fig. 9(a) where  $P(z) - G_l > 0$ . The form (3.12) describes the end result of the short time behavior of the hot-spot. A plot of  $v(z, \infty)$  defined in (3.12) is shown in Fig. 10 for the same parameter values as given in Fig. 9(a).

Since the solution to (3.12) is not continuous at the points  $z^*$  and  $1 - z^*$ , we must smooth out these discontinuities (see Fig. 10) by introducing diffusive layers of width  $O(\varepsilon)$  for the parabolic problem (3.9). These diffusive layers are not stationary but, instead, they evolve on a slow time scale

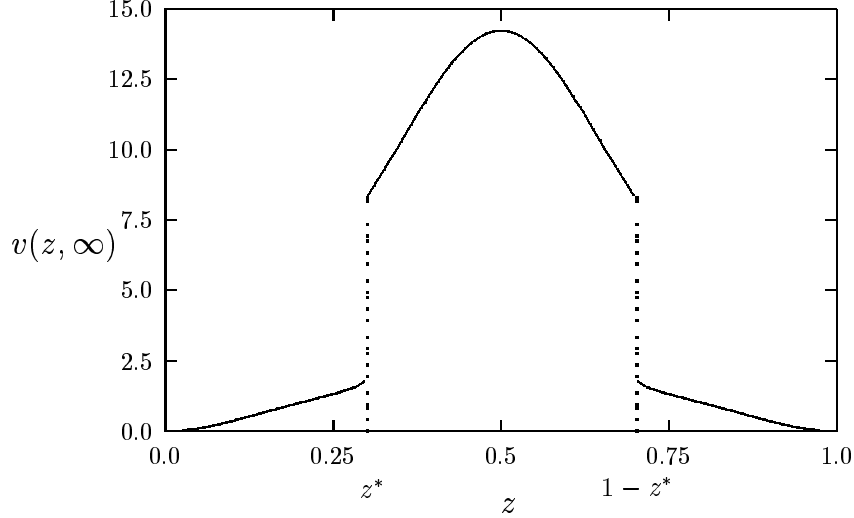


Figure 10: Plot of (3.12), which describes the initial hot-spot region, corresponding to the parameter values shown in Fig. 9a.

$\tau$  defined by  $\tau = \varepsilon\eta$ . By symmetry we need only consider the diffusive layer near the discontinuity at  $z = z^*$ .

To describe the evolution of the diffusive layer on  $z \in (0, 1/2)$ , which modulates the width of the hot-spot region, we proceed as in [4] for the case  $g(z) \equiv 1$ . We look for a solution to (3.9) of the form

$$v(z, \tau) \sim \begin{cases} v_l(z) & 0 < z < z_s(\tau), \\ \phi(\varepsilon^{-1}[z - z_s(\tau)]) & z = z_s(\tau) + O(\varepsilon), \\ v_u(z) & z_s(\tau) < z < 1/2, \end{cases} \quad (3.13)$$

where  $z_s(0) = z^* < 1/2$ . By symmetry, we can then use (3.13) to extend  $v$  to the entire interval  $(0, 1)$ . From (3.9a) and (3.13), we obtain that  $\phi(y)$  satisfies

$$\left(\kappa\phi'\right)' + \dot{z}_s[(\phi + 1)\Gamma]' + [P(z_s) - G(\phi)] \frac{f(\phi)}{g(z_s)} = 0, \quad -\infty < y < \infty, \quad (3.14a)$$

$$\phi(y) \rightarrow v_u(z_s), \quad y \rightarrow \infty; \quad \phi(y) \rightarrow v_l(z_s), \quad y \rightarrow -\infty; \quad \phi(0) = \frac{1}{2}[v_u(z_s) + v_l(z_s)], \quad (3.14b)$$

where  $\kappa = \kappa(\phi)$ ,  $\Gamma = \Gamma(\phi)$ , and  $\dot{z}_s \equiv dz_s/d\tau$ . The condition on  $\phi(0)$ , which eliminates the translation

invariance of (3.14a), is used to fix the location of  $z_s(\tau)$ . This problem, which is a nonlinear eigenvalue problem, is easily solved by COLSYS [1] to obtain  $\dot{z}_s$  as a function of  $z_s$ .

To obtain an ordinary differential equation for  $z_s$ , we multiply (3.14a) by  $\kappa\phi'$  and integrate from  $y = -\infty$  to  $y = \infty$  to get

$$\dot{z}_s(\tau) = H[z_s(\tau)], \quad \text{where} \quad H(z_s) \equiv [g(z_s)]^{-1} N(z_s)/D(z_s), \quad (3.15)$$

with  $z_s(0) = z^*$ . Here  $N(z_s)$  and  $D(z_s)$  are defined by

$$N(z_s) \equiv - \int_{v_l(z_s)}^{v_u(z_s)} [P(z_s) - G(\phi)] f(\phi) \kappa(\phi) d\phi, \quad (3.16a)$$

$$D(z_s) \equiv \int_{-\infty}^{\infty} \kappa(\phi) (\phi')^2 [\Gamma + \Gamma_\phi(1 + \phi)] dy. \quad (3.16b)$$

We assume that  $\Gamma = \Gamma(\phi)$  satisfies  $\Gamma + \Gamma_\phi(1 + \phi) > 0$  so that  $D(z_s) > 0$ . In the computations below we set  $\Gamma = 1$ . Notice that the numerator  $N(z_s)$  in (3.15) can be evaluated without solving (3.14). However,  $D(z_s)$  can only be obtained by computing the solution to (3.14).

We now discuss some qualitative properties of the dynamics of (3.15). The equilibrium value of  $z$  is obtained by setting  $N = 0$ . Writing  $N = N(P)$  instead of  $N = N(z_s)$ , this leads to the following equal area law that must be satisfied for a certain value of  $P$ :

$$\int_{v_l}^{v_u} [P - G(\phi)] f(\phi) \kappa(\phi) d\phi = 0. \quad (3.17)$$

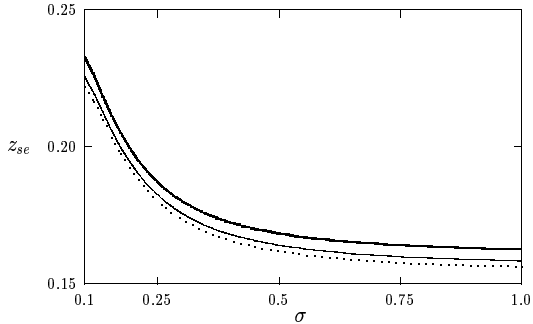
Here  $v_u$  and  $v_l$ , which depend on  $P$ , are the roots of  $P = G(\phi)$  corresponding to the upper and lower branches of  $G(\phi)$ , respectively. Since  $N(G_l) > 0$ ,  $N(G_m) < 0$ , and  $N'(P) > 0$  on  $G_m < P < G_l$ , it follows that there exists a unique root  $P = P_e$  to (3.17) on this interval. This value  $P = P_e$  is independent of the shape  $g(z)$  of the cross-section of the cylinder. Then, in terms of  $P_e$ , the equilibrium value of  $z_s(\tau)$ , denoted by  $z_{se}$ , satisfies the transcendental equation

$$P_e = P(z_{se}) \equiv pg(z_{se}) \sin^2(\pi z_{se}). \quad (3.18)$$

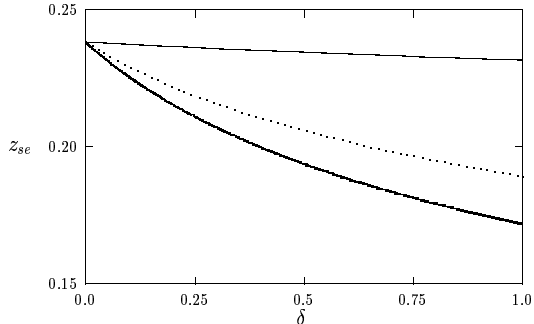
Since  $P(0) = 0$  and  $P(z)$  is monotonically increasing on  $(0, 1/2)$ , it follows that there exists a unique root to (3.18) with  $z_{se} < z^*$ . The monotonicity property of  $N(P)$  given above establishes that  $N < 0$  if  $z_{se} < z_s < z^*$ . Therefore, on this interval  $z_s(\tau)$  decreases monotonically towards  $z_{se}$  as  $\tau \rightarrow \infty$ .

Using Newton's method, we readily compute  $P_e$  for three different classes of conductivity function  $\kappa(u)$ . We take  $f(u)$  as given in (3.9d). We obtain,

$$\kappa(u) \equiv 1 \rightarrow P_e = 4.364; \quad \kappa(u) \equiv 1 + \frac{u^2}{2} \rightarrow P_e = 4.227; \quad \kappa(u) \equiv e^{-u/2} \rightarrow P_e = 4.628. \quad (3.19)$$



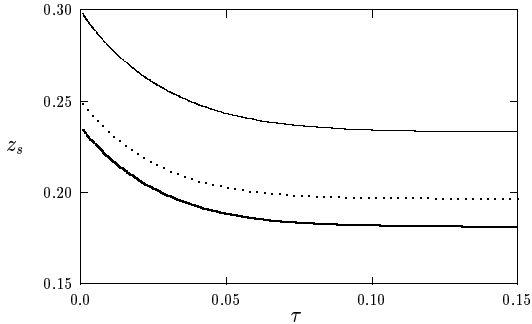
(a) Plot of  $z_{se}$  versus  $\sigma$ .



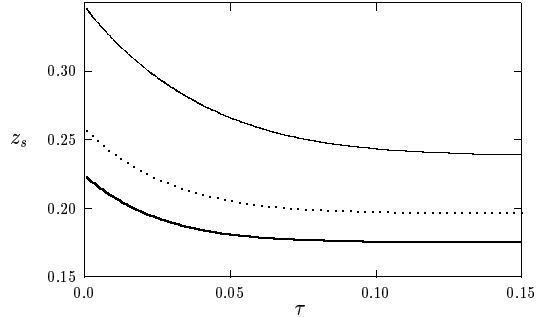
(b) Plot of  $z_{se}$  versus  $\delta$ .

Figure 11: In Fig. 11a we plot the equilibrium edge of the hot-spot  $z_{se}$  as a function of  $\sigma$  when  $a = 0.0$ ,  $\delta = 0.75$ , and  $p = 10$ . The solid curve corresponds to  $\kappa(u) = 1$ , the dotted curve corresponds to  $\kappa(u) = 1 + u^2/2$ , and the heavy solid curve corresponds to  $\kappa(u) = e^{-u/2}$ . In Fig. 11b we plot  $z_{se}$  versus  $\delta$  when  $\kappa(u) = e^{-u/2}$ ,  $a = 0$ , and  $p = 10$ . The solid, dotted, and heavy solid curves correspond to  $\sigma = 0.1$ ,  $\sigma = 0.25$ , and  $\sigma = 1.0$ , respectively.

Substituting  $P_e$  into (3.18) we determine  $z_{se}$ . Since the three values of  $P_e$  are within roughly 10%, we conclude that there is not a strong dependence of  $z_{se}$  on the conductivity model. This was observed for the case  $g(z) \equiv 1$  in [4]. In Fig. 11(a) we plot  $z_{se}$  versus  $\sigma$  for the three forms of  $\kappa(u)$ . The other parameter values are  $a = 0.0$ ,  $\delta = 0.75$ , and  $p = 10$ . Notice that as  $\sigma$  increases, then  $z_{se}$  decreases. Thus, physically, as the extent of the region where the cylinder is made thicker near  $z = 1/2$  increases, the hot-spot will propagate a greater distance towards the endpoints at  $z = 0$  and  $z = 1$  before reaching an equilibrium. In Fig. 11(b) we plot  $z_{se}$  versus  $\delta$  for three values of  $\sigma$ . We have taken  $\kappa(u) = e^{-u/2}$ ,  $a = 0$ , and  $p = 10$ . Notice, that when  $\sigma$  is very small,  $z_{se}$  is roughly constant as  $\delta$  is increased. Thus, if the cylinder is made considerably thicker near  $z = 1/2$ , but this region of thickness has a small spatial extent, then the hot-spot will become stationary at roughly the same position as it would have done for a circular cylinder of uniform thickness. Thus, for a hot-spot to propagate a large distance it is required that the cylinder be made thicker for a considerable range about the midpoint value  $z = 1/2$ . This is seen clearly in Fig. 12(a) where we plot the trajectories  $z_s$  versus  $\tau$  for several values of  $\sigma$  computed numerically from (3.14) and (3.15). In Fig. 12(b) we plot  $z_s$  versus  $\tau$  for several values of  $\delta$  at a fixed  $\sigma$ . Since  $\sigma = 0.5$  in this figure, which is not too small, the distance that the hot-spot propagates increases considerably as the amplitude  $\delta$  of the boundary deformation increases.



(a) Plots of  $z_s$  versus  $\tau$  for various  $\sigma$ .



(b) Plot of  $z_s$  versus  $\tau$  for various  $\delta$ .

Figure 12: In Fig. 12a we plot  $z_s$  versus  $\tau$  for three values of  $\sigma$  when  $\delta = 0.75$ . The solid, dotted, and heavy solid curves correspond to  $\sigma = 0.1$ ,  $\sigma = 0.25$ , and  $\sigma = 1.0$ , respectively. In Fig. 12b we plot  $z_s$  versus  $\tau$  for three values of  $\delta$  when  $\sigma = 0.5$ . The solid, dotted, and heavy solid curves correspond to  $\delta = 0.0$ ,  $\delta = 0.5$ , and  $\delta = 1.0$ , respectively. In both figures we have taken  $a = 0.0$ ,  $p = 10$ , and  $\kappa(u) = e^{-u/2}$ .

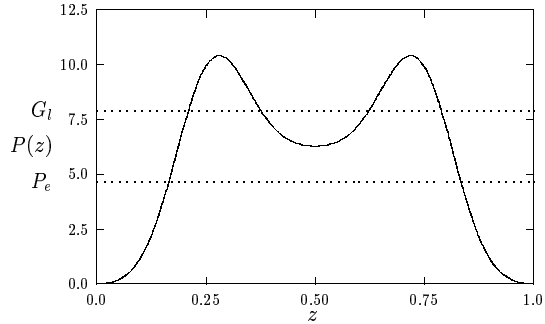
### 3.2 The Hot-Spot Solution: Case 2: $P(z)$ not monotone

When  $P(z)$  is not monotonic on  $(0, 1/2)$ , we have the possibility of multiple initial hot-spots. Every region where  $P(z)$  is greater than  $G_l$  corresponds to an initial hot-spot region. For a given boundary profile  $g(z)$ , there may be several disconnected regions where the condition  $P(z) > G_l$  is satisfied. In Fig. 13(a) we plot  $P(z)$  versus  $z$  for a set of parameters that gives two initial hot-spot regions. The parameters are  $\kappa(u) = e^{-u/2}$ ,  $p = 6$ ,  $\sigma = 0.1$ ,  $a = 0.32$ , and  $\delta = 1.4$ . The initial dynamics of the solution is given by (3.11). In this case, the solution  $v(z, \eta)$  to (3.11) has the long-time behavior

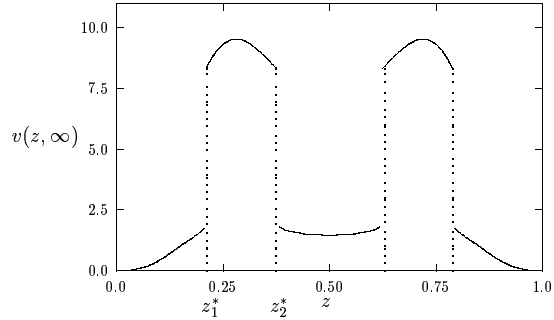
$$v(z, \eta) \rightarrow v(z, \infty) \equiv \begin{cases} v_l(z) & 0 < z < z_1^*, \\ v_u(z) & z_1^* < z < z_2^*, \\ v_l(z) & z_2^* < z < 1 - z_2^*, \\ v_u(z) & 1 - z_2^* < z < 1 - z_1^*, \\ v_l(z) & 1 - z_1^* < z < 1. \end{cases} \quad (3.20)$$

Here  $v = v_u(z)$  and  $v = v_l(z)$  are the upper and lower branches of  $P(z) = G(v)$ , respectively (see Fig. 8). Also,  $z_1^*$  and  $z_2^*$  are the two roots of  $P(z) = G_l$  on  $(0, 1/2)$  with  $z_1^* < z_2^*$ . A plot of  $v(z, \infty)$ , defined in (3.20), is shown in Fig. 13(b).

The initial hot-spot regions then begin to expand slowly, and diffusive layers near the disconti-



(a) Plot of  $P(z)$  versus  $z$ .



(b) Plot of initial hot-spot regions.

Figure 13: In Fig. 13a we plot  $P(z)$  versus  $z$  when  $\kappa(u) = e^{-u/2}$ ,  $p = 6$ ,  $\sigma = 0.1$ ,  $a = 0.32$ , and  $\delta = 1.4$ . In Fig. 13b we plot the initial hot-spot solution at the end of the transient period corresponding to Fig. 13a.

nuity points are needed. By symmetry we need only consider the interval  $z \in (0, 1/2)$ . Similar to the analysis in §3.1, we look for a solution to (3.9) on the interval  $(0, 1/2)$  of the form

$$v(z, \tau) \sim \begin{cases} v_l(z) & 0 < z < z_s(\tau), \\ \phi_1(\varepsilon^{-1}[z - z_{s1}(\tau)]) & z = z_{s1}(\tau) + O(\varepsilon), \\ v_u(z) & z_{s1}(\tau) < z < z_{s2}(\tau), \\ \phi_2(\varepsilon^{-1}[z_{s2}(\tau) - z]) & z = z_{s2}(\tau) + O(\varepsilon), \\ v_l(z) & z_{s2}(\tau) < z < 1/2, \end{cases} \quad (3.21)$$

where  $\tau = \varepsilon\eta$ ,  $z_{s1}(0) = z_1^*$ , and  $z_{s2}(0) = z_2^*$ . From (3.9a) and (3.20), we obtain that  $\phi_j(y)$  satisfies

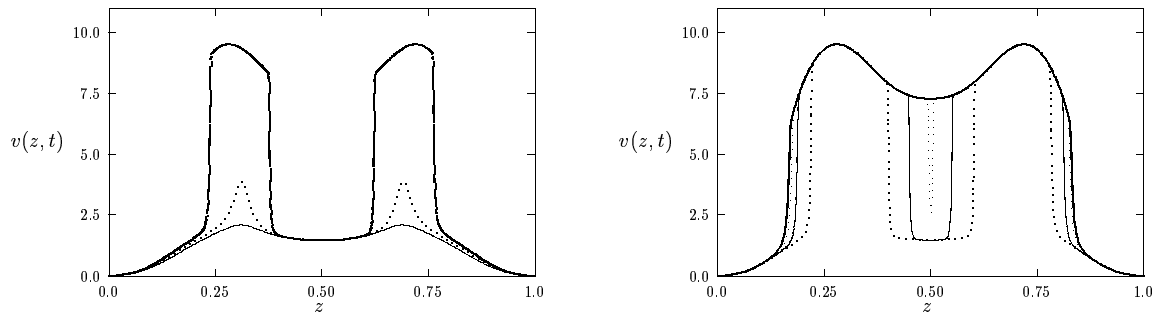
$$\left(\kappa\phi_j'\right)' + (-1)^{j-1}\dot{z}_{sj}[(\phi_j + 1)\Gamma]' + [P(z_{sj}) - G(\phi_j)]\frac{f(\phi_j)}{g(z_{sj})} = 0, \quad -\infty < y < \infty, \quad (3.22a)$$

$$\phi_j(y) \rightarrow v_u(z_{sj}), \quad y \rightarrow \infty; \quad \phi_j(y) \rightarrow v_l(z_{sj}), \quad y \rightarrow -\infty; \quad \phi_j(0) = \frac{1}{2}[v_u(z_{sj}) + v_l(z_{sj})], \quad (3.22b)$$

for  $j = 1, 2$ . In a similar way as in §3.1, we obtain that  $z_{sj}(\tau)$  satisfies the (uncoupled) ordinary differential equations

$$\dot{z}_{sj} = (-1)^{j-1}H[z_{sj}(\tau)], \quad (3.23)$$

for  $j = 1, 2$ . Here  $H(z_s)$  is defined in (3.15) in terms of  $N(z_s)$  and  $D(z_s)$  satisfying (3.16). Recall that the equilibrium value  $P_e$  satisfying  $N(P_e) = 0$  was independent of the boundary profile  $g(z)$ . The equilibrium values for (3.23) are obtained by setting  $P_e = P(z)$  and solving for  $z$ .



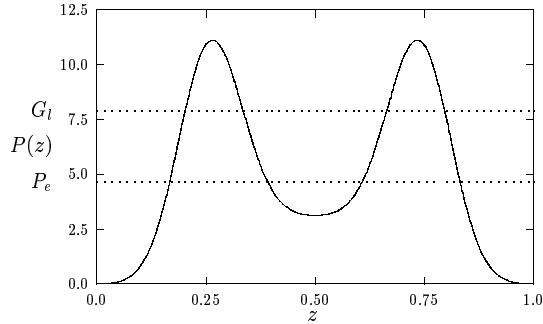
(a) Transient process of hot-spot formation.

(b) Evolution of the hot-spots and their merger.

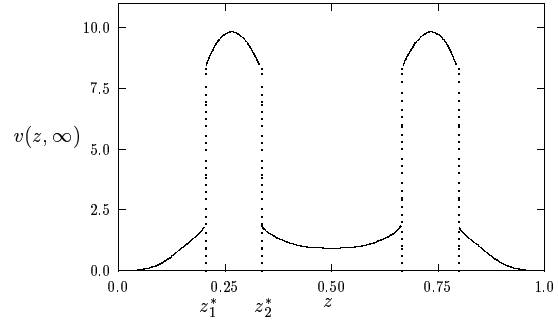
Figure 14: In these figures we plot the dynamical behavior for  $v$  for the parameter values given in Fig. 13 with  $\varepsilon = 0.02$ . In Fig. 14a we show the transient behavior describing the initial hot-spot formation. The solid, dotted, and heavy solid curves correspond to  $t = 1.01$ ,  $t = 1.28$ , and  $t = 2.01$ , respectively. In Fig. 14b we show the merger process leading to the steady-state solution. The dotted, solid, light dotted, and heavy solid curves correspond to  $t = 2.55$ ,  $t = 4.04$ ,  $t = 5.56$ , and  $t = 7.05$ , respectively.

In Fig. 13(a) we plot  $P_e$  on the graph  $P(z)$  versus  $z$ . In this case, there is only one equilibrium value  $z_{e1}$  on  $(0, 1/2)$ . Thus, we have that  $z_{s1} \rightarrow z_{e1}$  as  $\tau \rightarrow \infty$ . For the parameter values shown in Fig. 13(a), we compute numerically that  $z_{e1} = 0.165$ . However, the other interface centered at  $z_{s2}$  will increase monotonically as  $\tau$  increases. Eventually, it will cross the origin and collide with its mirror image located at  $z = 1 - z_{s2}$ . When  $z_{s2} - 1/2 = O(\varepsilon)$ , the analysis leading to (3.23) is no longer valid and a layer collapse phenomena occurs. The end result is that there is one large steady-state hot-spot region occupying the interval  $z \in (z_{e1}, 1 - z_{e1})$ . In Fig. 14(a), 14(b) we take  $\varepsilon = 0.02$  and we plot the numerical solution to (3.9) at different times for the parameter values of Fig. 13(a). These results were computed using the NAG library [12]. In Fig. 14(a) we show the transient behavior describing the initial formation of the hot-spot regions. In Fig. 14(b) we show the evolution of the diffusive interfaces, their merger at a later time, and the ultimate steady-state solution. This behavior is as predicted by the asymptotic theory.

To contrast this behavior, consider Fig. 15(a) where we plot  $P(z)$  versus  $z$  for another set of



(a) Plot of  $P(z)$  versus  $z$ .



(b) Plot of initial hot-spot regions.

Figure 15: In Fig. 15a we plot  $P(z)$  versus  $z$  when  $\kappa(u) = e^{-u/2}$ ,  $p = 3$ ,  $\sigma = 0.085$ ,  $a = 0.30$ , and  $\delta = 3.5$ . In Fig. 15b we plot the initial hot-spot solution at the end of the transient period corresponding to Fig. 15a.

parameter values. The initial hot-spot regions are shown in Fig. 15(b). In this case, the curve  $P(z)$  intersects  $P_e$  twice on  $(0, 1/2)$  and so there are two equilibrium values  $z_{e1}$  and  $z_{e2}$ . Thus,  $z_{sj} \rightarrow z_{ej}$  as  $\tau \rightarrow \infty$  for  $j = 1, 2$ . For the parameter values shown in Fig. 15(a), we compute numerically that  $z_{e1} = 0.167$  and  $z_{e2} = 0.392$ . In this case, the steady-state solution will be two disconnected hot-spot regions. For the parameter values shown in Fig. 15(a), in Fig. 16 we plot the numerical solution to (3.9) at different times computed using the NAG library. The heavy solid curve in Fig. 16 is very close to the steady-state solution. Notice that the two initial hot-spot regions remain disconnected as  $t$  increases. This phenomena where the diffusive wave gets blocked and cannot propagate to the other lobe of the dumbbell is qualitatively similar to the wave-blocking phenomena studied in [3], [7], and [13].

The general criterion that distinguishes between the behavior shown in these two examples is clear. Suppose  $P(z)$  is symmetric and has exactly one interior maximum on  $(0, 1/2)$ . Then, if  $\max[P(z)] > G_l$  and  $\min[P(z)] < P_e$ , there will be two initial hot-spots that will remain as disconnected regions as  $\tau \rightarrow \infty$ . This situation occurs when the domain is of dumbbell shape and the lobes of the dumbbell are sufficiently deep. Alternatively, if  $\max[P(z)] > G_l$  and  $\min[P(z)] > P_e$ , the two initially disconnected hot-spot regions will merge as  $\tau$  increases, producing one large steady-state region of elevated temperature.

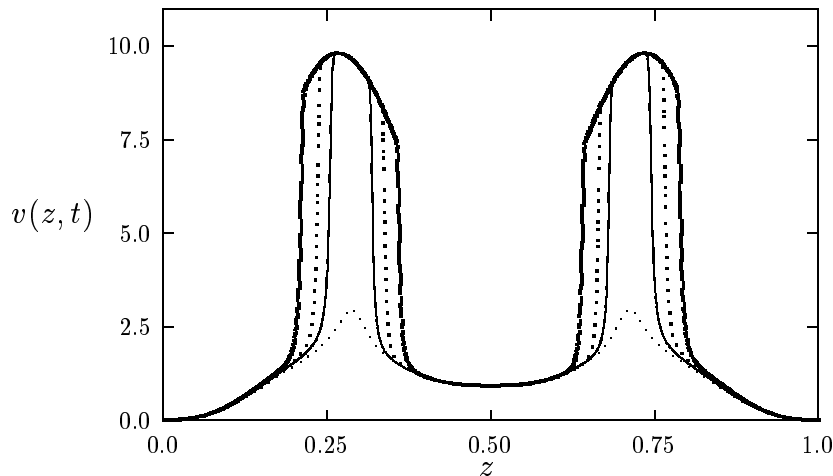


Figure 16: We plot the dynamical behavior of  $v$  for the parameter values given in Fig. 15a with  $\varepsilon = 0.02$ . The light dotted, solid, dotted, and heavy solid curves correspond to  $t = 2.53$ ,  $t = 3.03$ ,  $t = 3.54$ , and  $t = 4.55$ , respectively. The hot-spot regions remain disconnected for all time.

## Acknowledgements

I would like to thank the support of NSERC grant 81541 and the hospitality of the Mathematics Department at the City University of Hong Kong, where this paper was written. I also acknowledge the assistance of Cameron Connel, a former undergraduate student at UBC, with help on some preliminary numerical computations.

## References

- [1] U. Ascher, R. Christiansen, R. Russell, *Collocation Software for Boundary Value ODE's*, Math. Comp., **33**, (1979), pp. 659–679.
- [2] J. Bebernes, D. Eberly, *Mathematical Problems from Combustion Theory*, Appl. Math. Sciences, **83**, (1990), Springer-Verlag, New York.
- [3] J. Bell, C. Cosner, *Wave-like Solutions to Reaction-Diffusion Equations on a Cylinder: Dependence on Cylinder Width*, SIAM J. Appl. Math., **47**, No. 3, (1987), pp. 534–543.

- [4] M. Booty, G. Kriegsmann, *Microwave Heating and Joining of Ceramic Cylinders: A Mathematical Model*, Methods Appl. Anal., Vol. **4**, No. 1, (1994), pp. 403–414.
- [5] A. Bose, G. Kriegsmann, *Stability of Localized Structures in Nonlocal Reaction-Diffusion Equations*, Methods Appl. Anal., Vol. **5**, No. 4, (1998), pp. 351–366.
- [6] E. Eckert, R. Drake, *Heat and Mass Transfer*, McGraw-Hill, New York, (1959).
- [7] H. Ikeda, M. Mimura, *Wave-Blocking Phenomena in Bistable Reaction-Diffusion Systems*, SIAM J. Appl. Math., **49**, No. 2, (1989), pp. 515–538.
- [8] K. Gustafson, B. Eaton, *Exact Solutions and Ignition Parameters in the Arrhenius Conduction Theory of Gaseous Thermal Explosions*, Z. Angew. Math. Phys., **33**, (1982), pp. 392–405.
- [9] J. Kevorkian, J. D. Cole, *Multiple Scale and Singular Perturbation Methods*, Applied Mathematical Sciences, **114**, Springer, New York, (1996).
- [10] W. Kordylewski, *Critical Parameters of Thermal Explosion*, Combustion and Flame, **34**, (1979), pp. 109–117.
- [11] G. Kriegsmann, *Hot-Spot Formation in Microwave Heated Ceramic Fibres*, IMA J. Appl. Math., Vol. **59**, No. 2, (1997), pp. 123–148.
- [12] NAG Fortran library Mark 17, routine D03PCF, Numerical Algorithms Group Ltd. Oxford, United Kingdom (1995).
- [13] J. P. Pauwelussen, *Nerve Impulse Propagation in a Branching Nerve System: A Simple Model*, Physica D, Vol. **4**, No. 1, (1982), pp. 67–88.
- [14] G. Reimbert, A. A. Minzoni, N. F. Smyth, *Effect of Radiation Losses on Hotspot Formation and Propagation in Microwave Heating*, IMA J. Appl. Math. **57**, No. 2, (1996), pp. 165–179.
- [15] E. Van De Velde, M. J. Ward, *Criticality in Reactors under Domain or External Temperature Perturbations*, Proc. Roy. Soc. A, Vol. **434**, No. 1891, (1991), pp. 341–367.